A SEMI-EMPIRICAL MODEL OF THE WALL-NORMAL VELOCITY INDUCED BY FLOW-SHAPING PLASMA ACTUATORS

THESIS

Presented in Partial Fulfillment of the Requirements for Graduation with Distinction in the College of Engineering of The Ohio State University

By

Kevin James Disotell

Undergraduate Program in Aeronautical and Astronautical Engineering

The Ohio State University

2010

Honors Thesis Committee:

Professor James W. Gregory, Advisor

Professor Joseph H. Haritonidis

Abstract

Flow control devices are employed in aerodynamic applications to increase fluid momentum near the surface of a body moving through air. Flow-shaping plasma actuators are one example of a flow control device, and are aptly named for the spatial flow forcing achieved by a distribution of induced jets whose shape resembles the geometry of the electrodes which comprise the actuator. While much prior work has strived to model two-dimensional velocity profiles of single dielectric-barrier discharge actuators, the present study is aimed at the development of a semi-empirical framework to describe the induced jet velocity distribution for inherently three-dimensional configurations such as flow-shaping plasma actuators. The philosophy of the proposed model mirrors the underlying design principle for flow-shaping actuators – that the buried electrode geometry modulates the induced wall-normal velocity profile by limiting the extent of plasma formation. Approximations of potential flow and negligible end-effects are invoked. In the model, a single cross-section of the induced velocity profile is empirically acquired at the location of maximum interacting plasma volume and then modulated by a Fourier series expression of the lengthwise buried electrode geometry to produce the wall-normal velocity distribution. To validate this hypothesis, a buried electrode of square-wave geometry with length of 18-cm and spatial wavelength of 6-cm served as the test article. Experimental velocity data obtained with a pitot tube were compared to the spatial model and correlate well for a first-order engineering

approximation. It was also shown that the maximum induced velocity data follow a periodic distribution for the given square-wave electrode geometry. In a practical sense, the proposed model demonstrates a significant step toward simulating the fluid dynamics of flow-shaping actuators without the need to model the complex electromagnetic effects associated with their operation.

Dedication

To William J. Disotell, Darlene S. Disotell, Michael W. Disotell

and Diane V. Oyer-Meadows

Acknowledgments

I sincerely wish to thank my advisor, Dr. James Gregory, for the many opportunities he has afforded me in conducting research as an undergraduate and for his unselfish investment of time in developing me as an engineer and a person. I express my utmost gratitude and respect to him. To an equal degree, I also wish to thank Dr. Joseph Haritonidis, whose tutelage will forever have a presence in my career.

My family has always provided loving support for my endeavors, and I am truly blessed to have benefitted from their constant guidance. To my parents and late grandmother, I owe the privilege of receiving the sacred gift of education; I can only repay their sacrifices by sharing what light I have been given with others.

Finally, I am grateful to the Engineering Experiment Station in the Ohio State University College of Engineering for the financial support to conduct this work.

Vita

April 16, 1988 .....Born, Boardman, Ohio, USA

June 6, 2006 .....Boardman High School; Boardman, Ohio

June 13, 2010 .....B.S., Aeronautical and Astronautical Engineering, The Ohio State University

Fields of Study

Major Field: Aeronautical and Astronautical Engineering

Table of Contents

Table of Contents (ended)

List of Tables

List of Figures

List of Figures (ended)

Nomenclature

d	dielectric thickness
F	shaping function for buried electrode geometry
f	frequency of applied sinusoidal waveform
$g(x)$	functional equivalent of fundamental buried electrode geometry
g_a	gravitational acceleration at sea level
p	absolute pressure
T	absolute temperature
v	induced velocity cross-section normal to dielectric surface at (X, Z)
V	2-D induced velocity distribution normal to dielectric surface
Vpp	applied peak-to-peak AC voltage for sinusoidal waveform
w	buried electrode width
x	spanwise distance along buried electrode
y	height normal to buried electrode
z	distance from buried electrode centerline
X	x-station corresponding to maximum interacting plasma volume
Y	given height above dielectric surface at location X
Z	z-station corresponding to maximum interacting plasma volume
α_1, α_2, α_3, α_4	empirical coefficients from sum of exponentials curve fit
β	virtual electrode correction factor
Δp	dynamic pressure

λ_s	spatial wavelength of fundamental buried electrode geometry
ρ	air density

Subscripts

0	quantity at stagnation conditions
∞	quantity at free stream conditions

Chapter 1: Introduction

It has been demonstrated in many studies, both computational and experimental, that a body with spatial "waviness" is characterized by a smaller form drag coefficient compared to the same body with linear geometry.[1] Nature takes advantage of this aerodynamic property in the example of humpback whales, where their scalloped fins enable increased maneuvering performance in the ocean compared to their finned counterparts without such leading-edge bumps, as illustrated in Figure 1.[2]

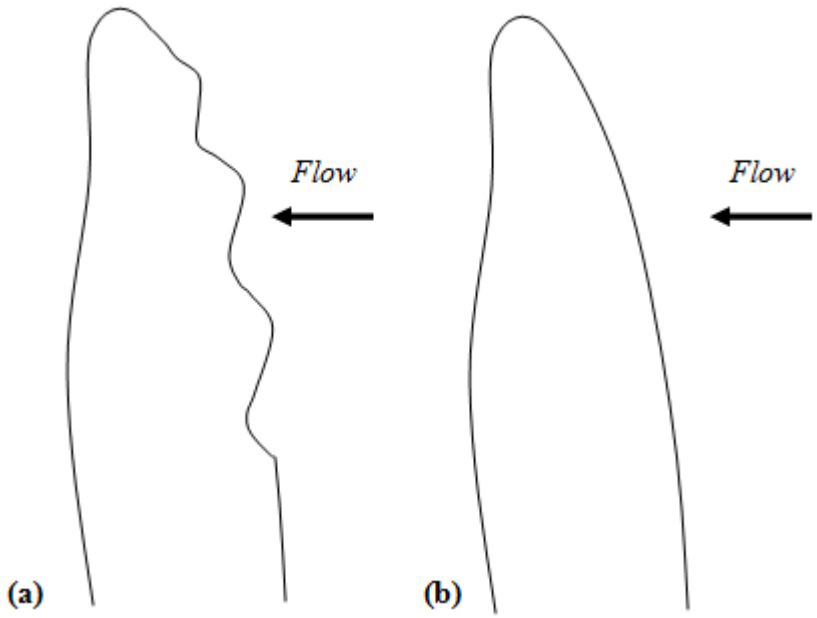

Figure 1: (a) Planform of humpback whale fin compared to (b) common fin.

The same observation is made in a fluid like air, where a right circular cylinder with surface "waviness" has a lower drag coefficient than its linear counterpart.[1] Because of

the associated increase in aerodynamic (and hydrodynamic) performance, spatial waviness has become an effective form of passive flow control. However, introducing these geometric modifications to existing structures is not without great cost.

Active Flow Control

Various forms of active flow control which can be retrofitted to a structure have been employed to mimic geometric waviness, such as surface suction and blowing, acoustic excitation, and surface heaters. These techniques, while proven to be effective, present great challenges for full-scale implementation. Recent developments in devices described as flow-shaping plasma actuators have made spatially-distributed flow forcing possible without complex installation requirements. The plasma actuator has no moving parts, negligible weight, and no mass flow demands for its operation. A schematic of the flow-shaping single dielectric barrier discharge (SDBD) plasma actuator is shown in Figure 2.

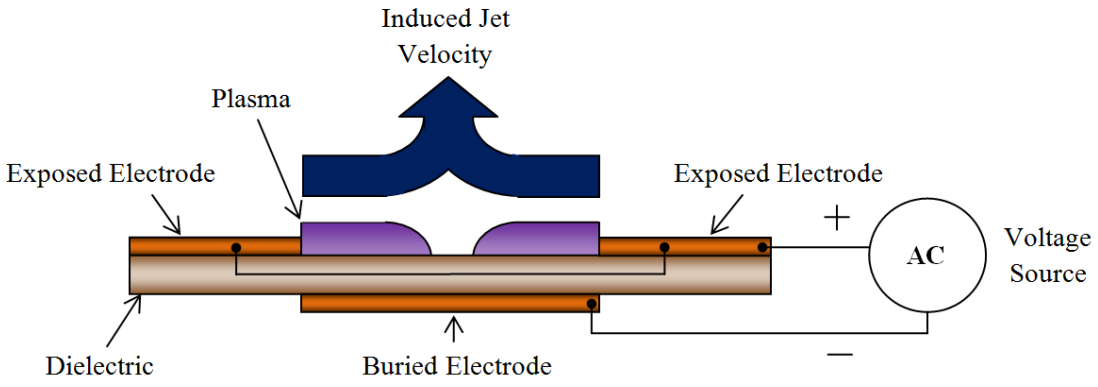

Figure 2: Schematic of flow-shaping SDBD plasma actuator.

Flow-shaping plasma actuators are comprised of two conventional SDBD actuators, each having a single exposed electrode, arranged in opposition to one another. The tangential wall jet produced near each exposed electrode combine to result in a jet which is normal to the dielectric surface.

Plasma actuators convert electrical energy from a high-voltage source to kinetic energy of the fluid; the requirement of an external energy source to do so qualifies the device as a form of active flow control. By applying a large potential difference between two electrodes identified as the exposed and buried electrodes, neutral air molecules near the exposed electrode become ionized. The ions are accelerated by the electric field and collide with ambient air molecules. As a result, a small jet is produced which can be used to delay boundary layer separation or induce vorticity. Flow-shaping plasma actuators modulate the spanwise velocity distribution according to the geometry of the buried electrode, due to the fact that the plasma is limited by the extent of the buried electrode.

Distributed Flow Forcing

Distributed forcing is more capable of manipulating three-dimensional structures in the flow, such as those observed in the canonical case of vortex shedding on a circular cylinder. In their computational study, Kim and Choi[3] simulated distributed forcing to study the effects of surface suction and blowing on the wake of a circular cylinder using two slots positioned 180° from each other. For the case of surface blowing, which is

similar to the flow motion induced by flow-shaping plasma actuators, the wall velocity distribution was simulated along the spanwise slot direction *x* as,

$$\phi_1(x) = \phi_{\max} \sin\left(2\pi \frac{x}{\lambda_s}\right) \tag{1}$$

$$\phi_2(x) = \phi_{\max} \sin\left(2\pi \frac{x}{\lambda_s} + \zeta\right)$$

where ϕ_1 and ϕ_2 were the radial velocities imposed on the top and bottom slots of the cylinder, respectively, $\phi_{\max}$ was the forcing amplitude varied as a percentage of the free stream velocity, λ_s was the wavelength of the imposed velocity distribution, and ξ was the phase difference between the upper and lower blowing profiles. Both in-phase ($\xi = 0$) and out-of-phase ($\xi = \pi$) forcing were simulated. Appreciable differences in the mean flow properties were observed for the in-phase forcing, resulting in a 20-25% reduction in drag.

Gregory *et al*.[4] followed with an experimental study in which flow-shaping actuators were employed to achieve the same suction and blowing profiles on a circular cylinder as in the work by Kim and Choi.[3] Tangential plasma forcing on the cylinder, which is analogous to surface suction, reduced the sectional drag coefficient by approximately 70%. Wall-normal forcing (analogous to surface blowing as opposed to

surface suction) exhibited significant control authority, increasing the sectional drag coefficient by approximately 60%.

Parameters Related to Plasma Actuator Operation

The level of control authority for plasma actuators is inherently influenced by the electrical properties of the device. Enloe *et al*.[5] and Pons *et al*.[6] modeled the SDBD electrical discharge phenomena as a lumped-element RC circuit. In doing so, a better understanding of the relationships among discharge parameters such as voltage, surface charge, and power dissipated by the actuator was grasped. The dissipated power differed by less than 6% between the circuit model and experimental data. Moreover, Enloe *et al*.[5] contributed the important result that the maximum induced velocity for a SDBD actuator is proportional to the seven-halves power of applied AC voltage (and therefore dissipated electric power), regardless of waveform shape. While the discharge properties of plasma actuators have been studied diligently, the geometric effects of electrode design have only been investigated on a parametric basis. Enloe *et al*.[5] also reported the interesting fact that the bulk properties of the plasma discharge are independent of the exposed electrode width, yet strongly dependant on thickness. They layered copper tape to vary the thickness of the exposed electrode and used steel wire of different diameters to conclude that a thinner exposed electrode results in a higher rate of momentum transfer to the neutral air. Moreover, the cross-sectional geometry, whether a square piece of tape or circular wire, was proven to have negligible effect on the momentum transfer due mainly to the effect of Debye shielding.

Semi-Empirical Modeling

Hall *et al*.[7] invoked potential flow assumptions to replicate the effects of an asymmetric, SDBD actuator as a doublet flow. A NACA 0009 airfoil was tested at two free stream velocities of 15 and 30 m/s with the plasma actuator installed at approximately 75% chord on the upper airfoil surface. The objective of the model was to replace the actuator with a doublet in a Smith-Hess panel code, where existing experimental data for a given actuator design was input to calibrate the strength of the doublet. In this way, the circulation induced with the effect of the plasma actuator could be calculated using the panel code. The merits of this work included solely modeling the fluid dynamics of the actuator without the associated electromagnetic effects, but also reflected the current need for experimental input if the actuator is to be modeled with sufficient accuracy. The doublet model proved to be an efficient first-order approach for engineering analysis of SDBD actuators used as lift augmentation devices on wing sections.

Modeling Flow-Shaping Plasma Actuators

For flow-shaping actuators, the geometry of the buried electrode is inextricably linked to the discharge properties; the two must necessarily be treated together in studying the induced velocity distribution. To this end, modeling the full interaction between the ambient fluid and the plasma has proven to be a rigorous undertaking. A viable computational model of the plasma actuator must account for the spatial and

temporal details of the plasma physics, including an accurate description of the electric field that is strongly tied to the electrode shape. Consequently, only a few simple geometries have been tractable, such as a layer of plasma between two infinite planes, two right circular cylinders, and two spheres.[8] A computationally viable model of the SDBD actuator was recently contributed by Orlov and his colleagues[9,10] who developed a space-time lumped-element model of the two-dimensional, wall-tangential actuator configuration. However, the model has yet to be extended to flow-shaping configurations.

Based on the aforementioned complexities, the need for a first-order approximation of the induced velocity distribution for flow-shaping plasma actuators is necessary for design optimization. The aim of the present work is to develop an appropriate engineering model to describe the large-scale interaction of the induced plasma jets with the ambient fluid.

Chapter 2: Modeling Hypothesis

Binary Plasma Actuator

As originally studied by Porter *et al.*[11], the binary plasma actuator produces an array of jets shaped by a buried electrode of square-wave geometry, similar to the "on-off" nature of a binary (digital) signal. Figure 3 shows a schematic of the nominal wall-normal velocity distribution along the centerline of the binary buried electrode.

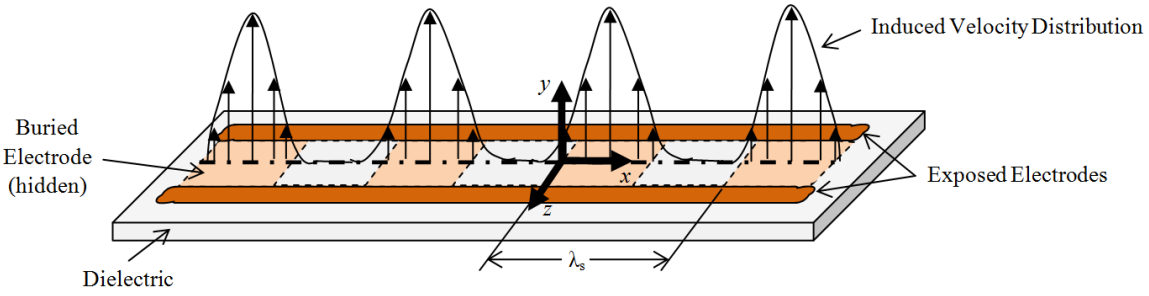

Figure 3: Spatial array of jets formed by binary plasma actuator.

In a sense, the binary actuator is comprised of two SDBD actuators, each having a single exposed electrode, facing one another with periodic regions of the shared buried electrode removed. The centerline of the buried electrode is the location at which the induced velocity is expected to be normal to the dielectric surface. Moreover, the maximum induced wall-normal velocity is expected to occur at the local region of maximum interacting plasma volume.[13] For a given square region where the buried electrode is present, the geometric center of the square is the location of maximum

interacting plasma volume. Due to the inherently unsteady microdischarge phenomena occurring at the edge of each exposed electrode, the induced velocity close to the exposed electrodes is essentially tangential to the surface.[12] Because the binary actuator represents a simple geometry to study, the induced wall-normal velocity along the centerline of the binary actuator will be investigated in this work, as this is the most meaningful velocity component for the given design.

The fundamental flow property to be modeled in this work is the induced velocity. The body force may be obtained from conservation of momentum using a control volume approach. As always, a desirable model of any given flow-shaping actuator will have the properties of computational efficiency and accuracy to the observed phenomena. Since the theoretical underpinnings of the plasma actuator physics have proven to be quite complex (and generally intractable), a semi-empirical model will be set forth with the objective of determining the induced velocity magnitude normal to the dielectric surface in quiescent air as a function of spatial coordinates x and y. For implementation in a computational fluid dynamics package, it may be possible to modify the model to a form similar to the radial blowing profiles in Equation 1 using the maximum induced velocity as the forcing amplitude. This will be discussed in Chapter 5.

Modeling Equations

The model at hand rests upon the philosophy that the induced velocity cross-section corresponding to the location of maximum plasma-volume interaction is spatially modulated by the buried electrode geometry. Moreover, it will be assumed that the time-

averaged interaction of the plasma with the ambient fluid is steady. These two statements are represented mathematically in the form of the algebraic equation describing the spanwise velocity distribution *V* given by (2),

$$V(x, y) = F(x) \cdot v(X, y, Z) \tag{2}$$

where the buried electrode geometry is expressed as a shaping function *F* and the cross-sectional velocity profile *v* as a function of the height coordinate normal to the dielectric surface is empirically obtained at the location of maximum interacting plasma volume (*X*, *Z*) where the maximum induced velocity is expected to occur. In the determination of a suitable function for *F*, it was surmised that any arbitrary, spatially-periodic buried electrode configuration may be represented as a periodic extension of its fundamental buried electrode geometry in the form of a Fourier series.

Determination of Shaping Function

The determination of the Fourier series describing the buried electrode geometry will be carried out for the binary actuator, with the reference coordinate system and length parameters shown in Figure 4.

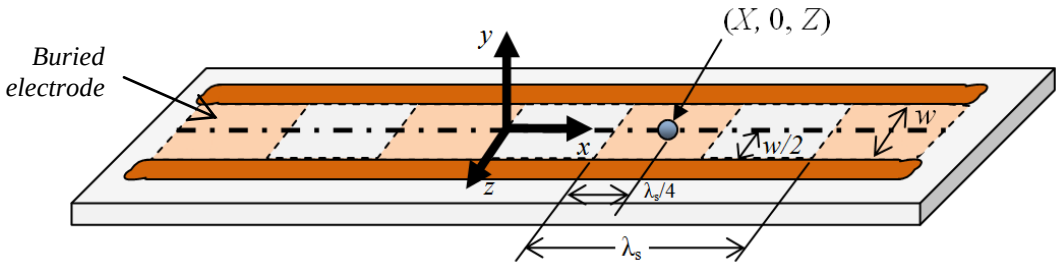

Figure 4: Schematic of binary plasma actuator with annotated coordinate system.

Figure 5 illustrates the conversion of the physical buried electrode geometry to its equivalent piecewise function $g(x)$, which is periodically extended via its Fourier series description. One edge of the buried electrode is aligned with the horizontal axis of the Cartesian coordinate system so that a cut-out region of electrode has a functional value $g = 0$.

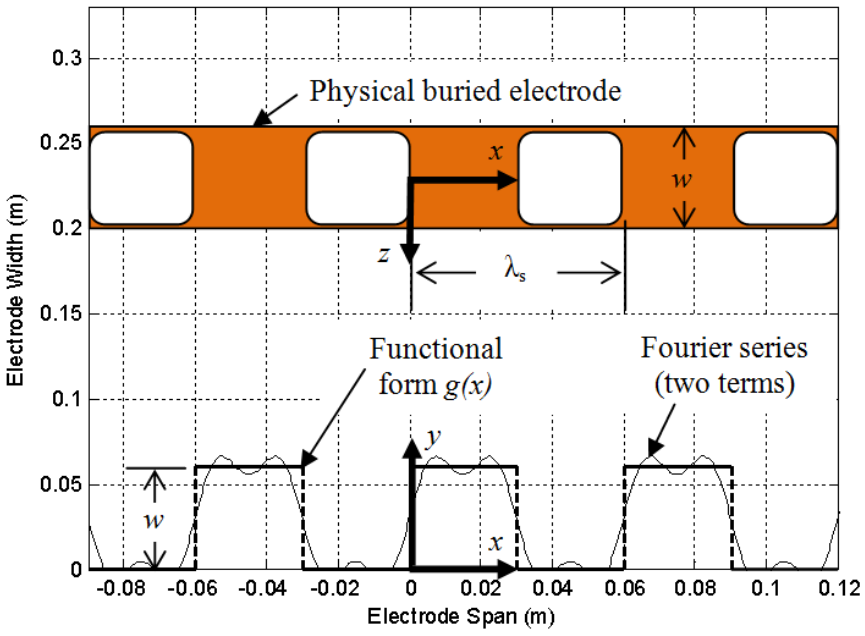

Figure 5: Fourier series for binary buried electrode geometry (λ_s = 6 cm).

The physical binary buried electrode is converted to its square-wave equivalent $g(x)$, which may be expressed as a piecewise function given by (3),

$$g(x) = \begin{cases} 0 & -\lambda_s/2 < x < 0 \\ w & 0 < x < \lambda_s/2 \end{cases} \tag{3}$$

The square-wave function representing the buried electrode geometry is then expressed as a Fourier series given by (4),

$$F(x) = a_0 + \sum_{n=1}^{\infty} a_n \cos\left(n\pi \frac{x}{L}\right) + b_n \sin\left(n\pi \frac{x}{L}\right) \tag{4}$$

where the coefficients a_0, a_n, and b_n ($n = 1, 2, 3, \ldots$) are given by the Euler formulas in (5a), (5b), and (5c):

$$a_0 = \frac{1}{2L} \int_{-L}^{L} g(x)dx \tag{5a}$$

$$a_n = \frac{1}{L} \int_{-L}^{L} g(x) \cos\left(n\pi \frac{x}{L}\right) dx \tag{5b}$$

$$b_n = \frac{1}{L}\int_{-L}^{L} g(x)\sin\left(n\pi\frac{x}{L}\right)dx \tag{5c}$$

For a geometric period (spatial wavelength) of λ_s, $L = \lambda_s/2$ for the given form of the Fourier series. In this way, the Fourier coefficients for the binary actuator are found from (5a), (5b), and (5c) to be $a_0 = w/2$, $a_n = 0$, and $b_n = \frac{w}{n\pi}\left\{(-1)^{n+1}+1\right\}$. Therefore, the Fourier series of the binary buried electrode geometry is:

$$F(x) = \frac{w}{2} + \sum_{n=1}^{\infty}\frac{w}{n\pi}\left\{(-1)^{n+1}+1\right\}\sin\left(2n\pi\frac{x}{\lambda_s}\right) \tag{6}$$

Several notes must be made in regard to the Fourier series and its inclusion in the proposed model given by (2). First, the number of terms to which the summation in (6) is carried out will certainly affect the shape of the velocity distribution; as the number of terms increases, the distribution will have *n* local maxima. In the case of the binary actuator, a single term in (6) is sufficient to describe the square-wave buried electrode, since the maximum induced velocity is expected to occur at the geometric center of a given square region where the electrode is present. For more elaborate geometries, a greater number of terms may be necessary; however, the present study will focus on applying the proposed framework to the binary actuator. Furthermore, the Fourier series

will incorrectly skew the acquired cross-sectional velocity data when the two components are multiplied according to the model in Equation 2 unless Equation 6 is normalized by the buried electrode width *w*. Therefore, after dividing through by *w*, Equation 6 becomes:

$$F(x) = \frac{1}{2} + \frac{2}{\pi}\sin\left(2\pi\frac{x}{\lambda_s}\right) \tag{7}$$

Finally, if a Fourier series is to be used as the shaping function, it will be shown in the following experimental data that the functional equivalent of the buried electrode geometry *g* must account for fluid interaction above regions where a portion of the electrode is not present. This model correction will be offered and explained in Chapter 4. The process of obtaining the second component of the model given in Equation 2, namely the measured cross-sectional velocity at the station of maximum interacting plasma volume, will also be described in Chapter 4 by a curve-fit to the acquired velocity data.

Chapter 3: Experimental Methodology

The binary actuator in this work was characterized by a buried electrode spatial wavelength of λ_s = 6 cm, spanning a length of 18 cm with a width of 6 cm. Both the buried electrode and exposed electrodes were fabricated from thin copper tape, and both electrodes were of the same thickness (0.07 mm). The dielectric used was mica, with a dielectric strength of 300 kilovolts per inch and relative permittivity of 7 farads per meter; the two dielectric thicknesses tested were 0.183 cm and 0.213 cm.

Plasma-Generating Circuit

A high-voltage AC circuit was wired to operate the plasma actuator. A wiring diagram of the circuit is shown in Figure 6. A signal generator is used to apply a small AC voltage (2-5 Vpp) to the circuit which is then stepped-up by the power amplifier (Crown XTI-2000) and high-voltage transformer. The plasma circuit was characterized by input voltage and frequency for the purposes of this study. Although the electrical discharge properties of the plasma actuator depend on the shape of the applied waveform from the signal generator, only a sine wave was applied to the circuit. A high-voltage probe was used to measure the applied peak-to-peak voltage across the actuator for several voltage settings on the signal generator; negligible resistance was assumed for the electrodes. Figure 7 shows the mapping between the applied actuator voltage and the voltage set on the signal generator (i.e., the input).

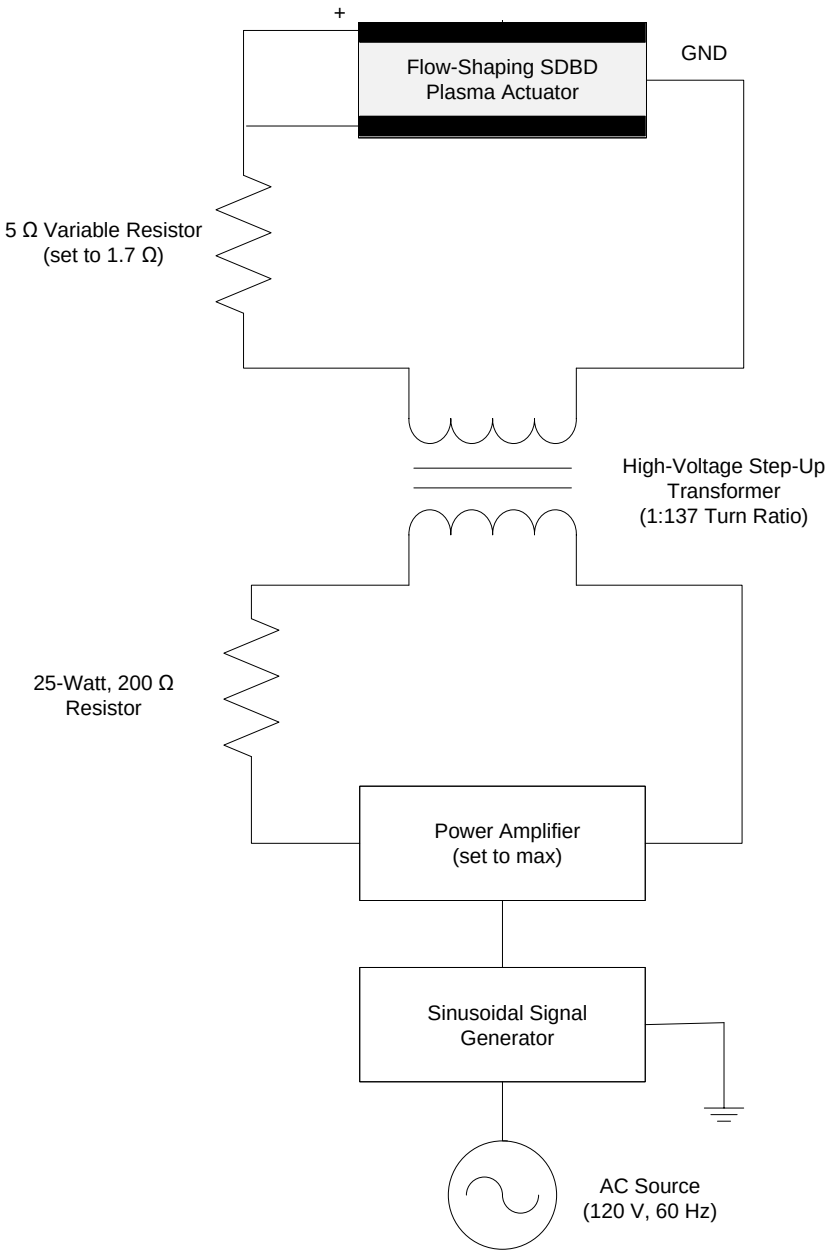

Figure 6: Wiring diagram for high-voltage AC circuit.

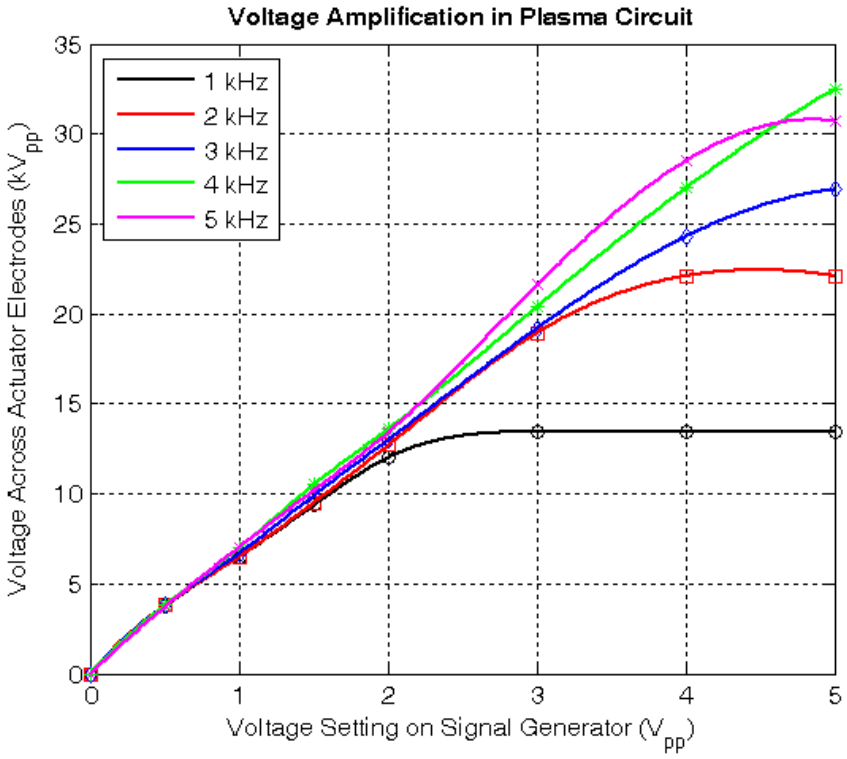

Figure 7: Voltage gain characteristics for plasma circuit with frequency as parameter.

The applied voltage is relatively independent of frequency up to approximately 7.5 kVpp. Asymptotic behavior characterizes the curves at higher applied voltages for a given frequency, which is owed to electromagnetic saturation of the high-voltage transformer's iron core. Saturation is alleviated by increasing the waveform frequency. The linear behavior of the voltage curve for 4 kHz is caused by the magnetic resonance frequency of the transformer, which is specified as 4 kHz for the particular model in the circuit (Corona Magnetics CMI-5530).

Instrumentation

Using an Agilent 33220A function generator to drive the AC circuit, a sinusoidal waveform was applied at frequencies between 3 and 5 kHz with peak-to-peak voltages ranging between 20 and 29 kVpp. A pitot tube was used to measure the total jet pressure in quiescent air at regularly-spaced points of 0.3 cm normal to the actuator surface. Cross-sectional velocity data were acquired at the geometric midpoint of the buried electrode, with the actuator placed inside a partially-sealed glass enclosure. The setup is illustrated in Figure 8, with the inset describing the location of the point on the actuator above which data was acquired. The pitot tube was fashioned from a capillary tube with an outer tip diameter of 1.5 mm. To alleviate problems with electromagnetic interference corrupting the transducer data, approximately 3 m of Tygon tube connected the pitot tube and pressure transducer in order to provide sufficient separation. The differential pressure transducer was an Omega PX274 low-pressure model (0-0.1 inches of water, +/- 1% full-scale accuracy) which was sampled by a National Instruments USB-6008 DAQ device. The sampling rate was 1 kHz, and pressure data were acquired for 30 seconds in each record.

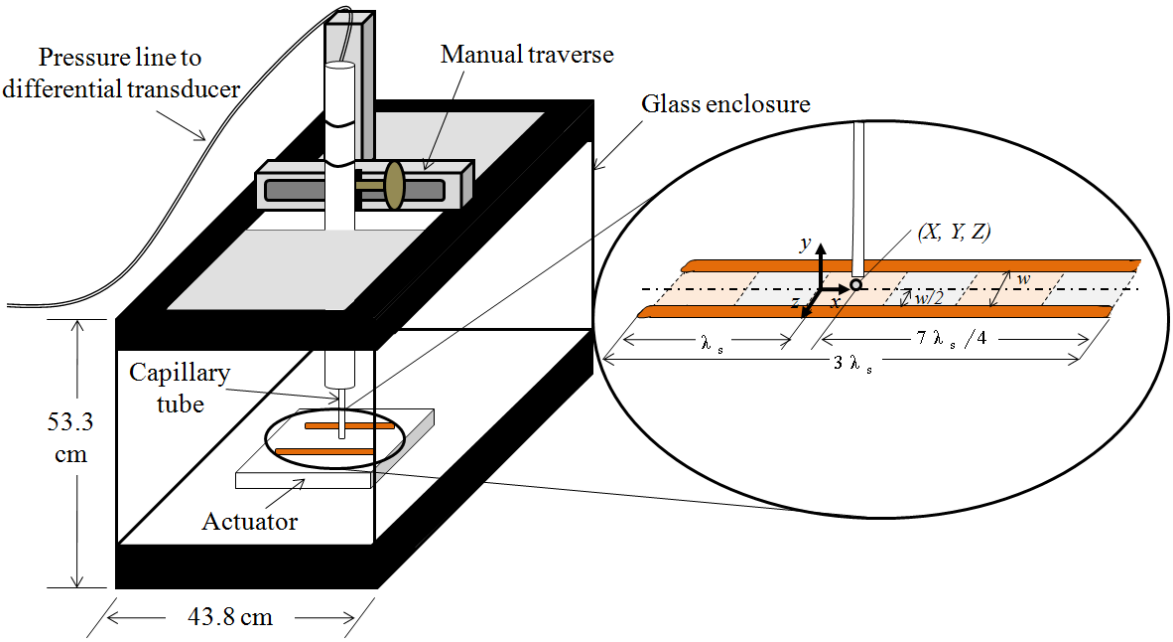

Figure 8: Experimental setup for velocity measurements in quiescent air.

Data Analysis

Under the simplifications of steady, incompressible flow, the induced velocity at a given height *Y* normal to the location of maximum interacting plasma volume is described by Bernoulli's equation applied along a streamline of the flow,[14]

$$p(X,Y,Z)+\frac{1}{2}\rho_{\infty}v(X,Y,Z)^{2}+\rho_{\infty}g_{a}Y=p_{0} \tag{8}$$

Neglecting the third term in (8) accounting for gravitational body force, the equation is rearranged for the induced velocity *v*:

$$v(X,Y,Z) = \sqrt{\frac{2\,\Delta p(X,Y,Z)}{\rho_\infty}} \tag{9}$$

Dynamic pressure data were acquired from the pressure transducer for thirty seconds and the mean value was taken for calculation in (9). The ambient density was calculated from the perfect gas law,

$$\rho_\infty = \frac{p_\infty}{RT_\infty} \tag{10}$$

Data Repeatability

Plots showing the effect of acquisition time on the measured velocity repeatability are included in Appendix A. Figure 9 shows the strong repeatability obtained with a time record of 30 seconds while data are acquired at the geometric center of the binary buried electrode. Note that the data presented here are for a dielectric material of fiberglass tape, and only serve to demonstrate the validity of the data processing technique.

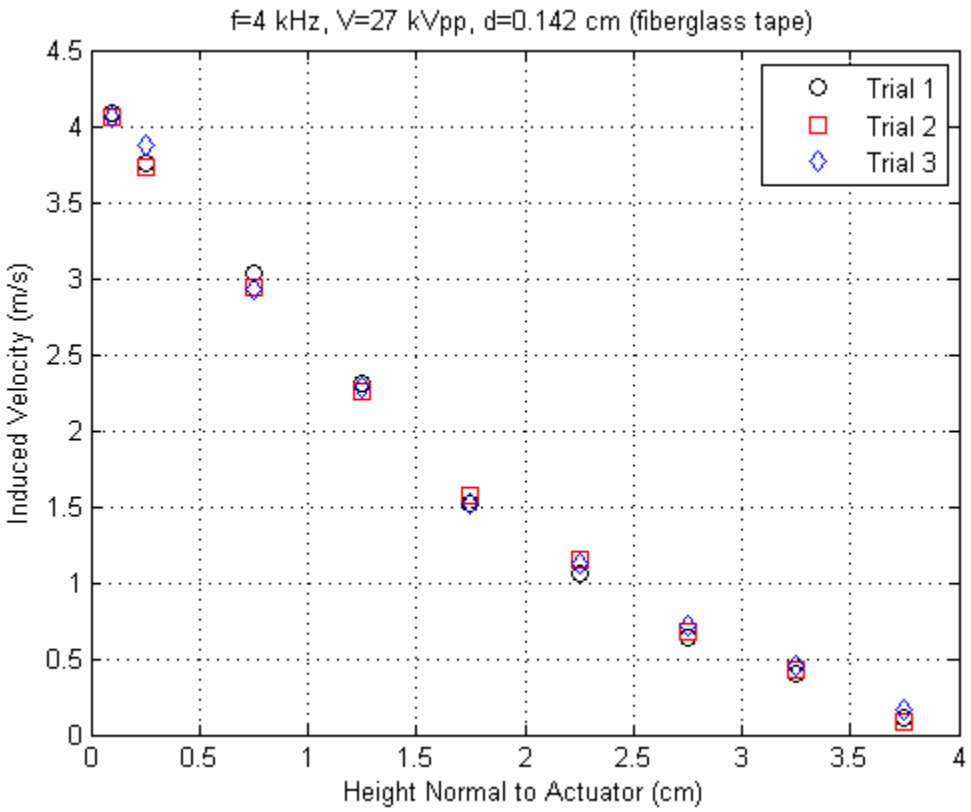

Figure 9: Repeatability for center electrode station, 30 sec time record (27 kVpp).

Chapter 4: Model Analysis

In the following sections, the method for obtaining the empirical data required as input to the proposed model is described and the results of the model are compared to experimental values. The presented velocity data sets were acquired at nearly the same nominal conditions among trials: temperature of 297 K, ambient pressure of 98.9 kPa, and ambient air density of 1.2 kg/m^3.

Curve Fitting of Cross-Sectional Velocity Data

Cross-sectional velocity data were acquired for two different driving frequencies (4 and 5 kHz) and dielectric thicknesses (0.183 and 0.213 cm) with applied voltage as a parameter. On the basis of "goodness of fit" statistics (namely, the adjusted R^2 value), the data were found to be well-described by a sum of exponentials,

$$v(X, y, Z) = \alpha_1 \exp(\alpha_2 y) + \alpha_3 \exp(\alpha_4 y) \tag{11}$$

where the coefficients α_1, α_2, α_3, and α_4 were determined for each data set using Mathworks Curve Fitting Toolbox 2.0. Table 1 compares the values of these coefficients for a constant applied voltage of 27 kVpp among three data sets.

Table 1: Coefficients from sum of exponentials fit for applied voltage of 27 kVpp.

	***f* = 4 kHz, *d* = 0.183 cm**	***f* = 5 kHz, *d* = 0.183 cm**	***f* = 5 kHz, *d* = 0.213 cm**
α_1	3.603	1.04	-424606.798
α_2	-1.329	-1.35	-3.4326
α_3	-3.602	-0.025	424606.797
α_4	-9.536	-3.957	-3.4325

The coefficient values in Table 1 do not appear to lend themselves to a physical interpretation of parameters related to operation of the plasma actuator: the order of magnitude and even signage varies considerably. The coefficients for f = 5 kHz, d = 0.213 cm reflect a tenuous curve fit, as the numerical values must be carried out to the thousandths or even ten-thousandths decimal place to avoid the case where $\alpha_1 = \alpha_3$, $\alpha_2 = \alpha_4$. Fit statistics for the corresponding data sets in Table 1 are presented in Table 2, and show a strong correlation reflected in the R^2 value and the sum of squares due to error (SSE).

Table 2: Curve fit statistics for three data sets with applied voltage of 27 kVpp.

	***f* = 4 kHz, *d* = 0.183 cm**	***f* = 5 kHz, *d* = 0.183 cm**	***f* = 5 kHz, *d* = 0.213 cm**
SSE	0.04224	0.1788	0.02589
R^2	0.9941	0.9816	0.9945

The general effects of applied voltage, driving frequency, and dielectric thickness on the induced velocity profile are captured by Figure 10, Figure 11, Figure 12.

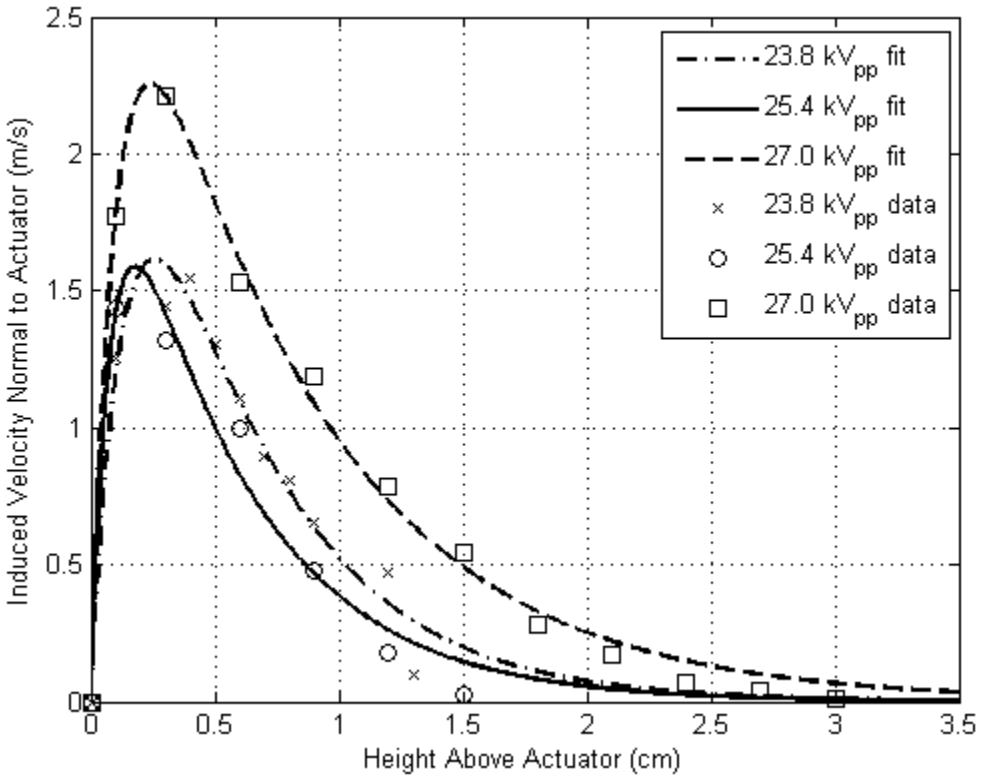

Figure 10: Cross-sectional velocity data for 4 kHz driving frequency (d=0.183 cm).

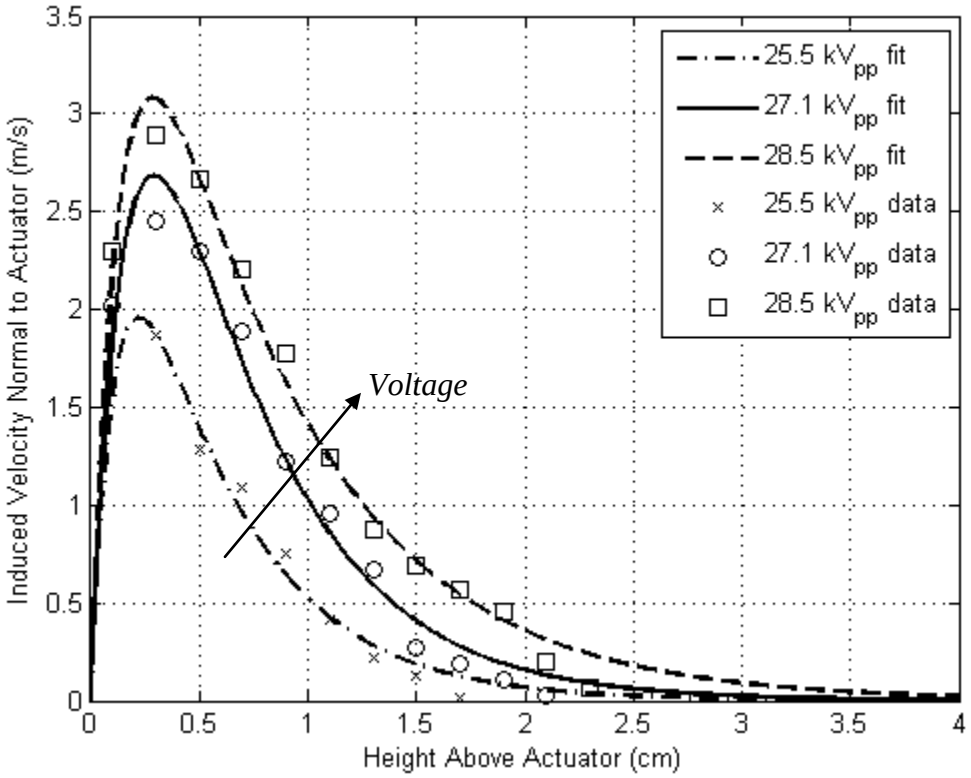

Figure 11: Cross-sectional velocity data for 5 kHz driving frequency (d=0.183 cm).

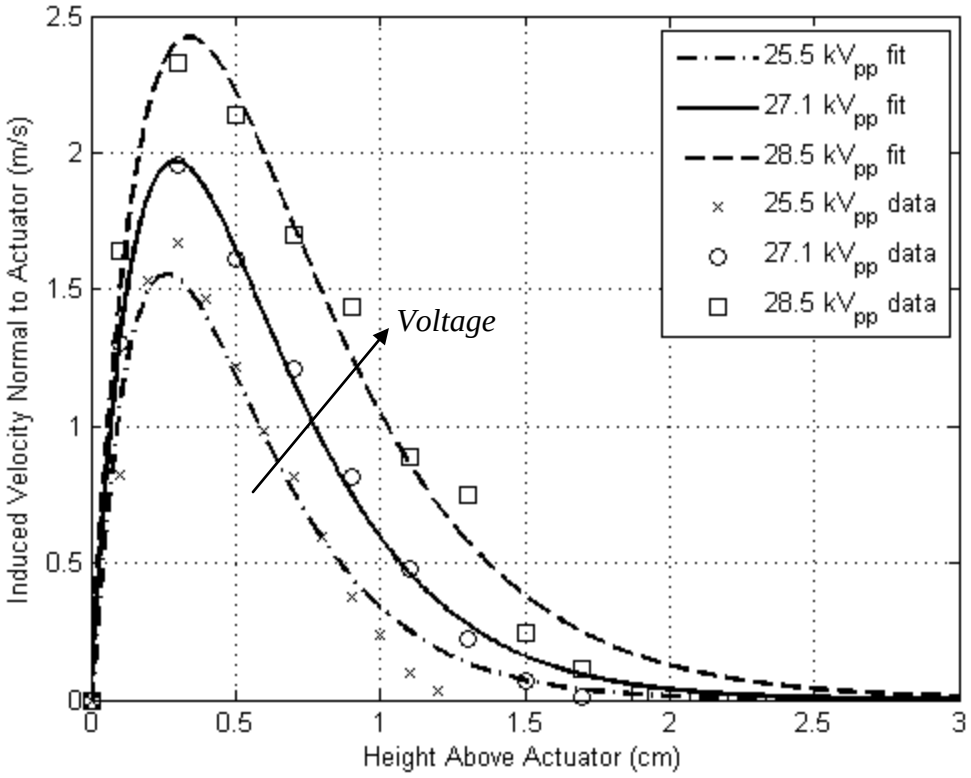

Figure 12: Cross-sectional velocity data for 5 kHz driving frequency (d=0.213 cm).

All other quantities being equal, the maximum induced velocity tends to increase with applied voltage. The induced velocity is higher for larger driving frequencies, and decreases with a thicker dielectric.

Spanwise Velocity Data

In order to compare the accuracy of the proposed model to the actual spanwise variation of the velocity distribution, a grid of 117 data points (13 equally-spaced vertical

points per station for 9 spanwise stations) were acquired along the centerline of the buried electrode. The vertical spacing of the data points was 0.3 cm, and the spanwise stations were spaced 0.75 cm apart. The region of buried electrode near the center of the span was chosen to acquire data, since this would reduce the influence of end-effects on the velocity distribution. The origin of the coordinate system shown in the inset of Figure 8 will be referenced in the following data sets. Data were acquired between $x = -\lambda_s/2$ to $x = +\lambda_s/2$, inclusively, and then linearly interpolated at points between these values. Figure 13 presents the velocity contours for the set of electrical parameters $f = 4$ kHz, $d = 0.183$ cm, and applied voltage of 27 kVpp; the diagram beneath plot shows data plane and corresponding buried electrode region. The data set in contained in Table 3 of Appendix A for reference.

As Figure 13 shows, the maximum induced velocity approximately corresponds to the midpoint of the electrode spanning the region $0 < x < 3$ cm. This midpoint ($x = 1.5$ cm) is the location of maximum plasma volume interaction as expected, occurring less than 5 mm above the wall. However, in the region where the electrode is cut out ($-3 < x < 0$ cm), there is still enough plasma-fluid interaction to result in a relatively large induced velocity. Upon capturing an image of the binary plasma actuator while in operation, as shown in Figure 14, it may be the case that the small strips of copper tape required to preserve electrical continuity on the buried electrode actually yield a sufficient amount of plasma-fluid interaction to create an induced velocity normal to the dielectric surface. On the other hand, it could be that the adjacent plasma jets entrain fluid in the cut-out electrode region as a result of the vorticity induced by the actuator.

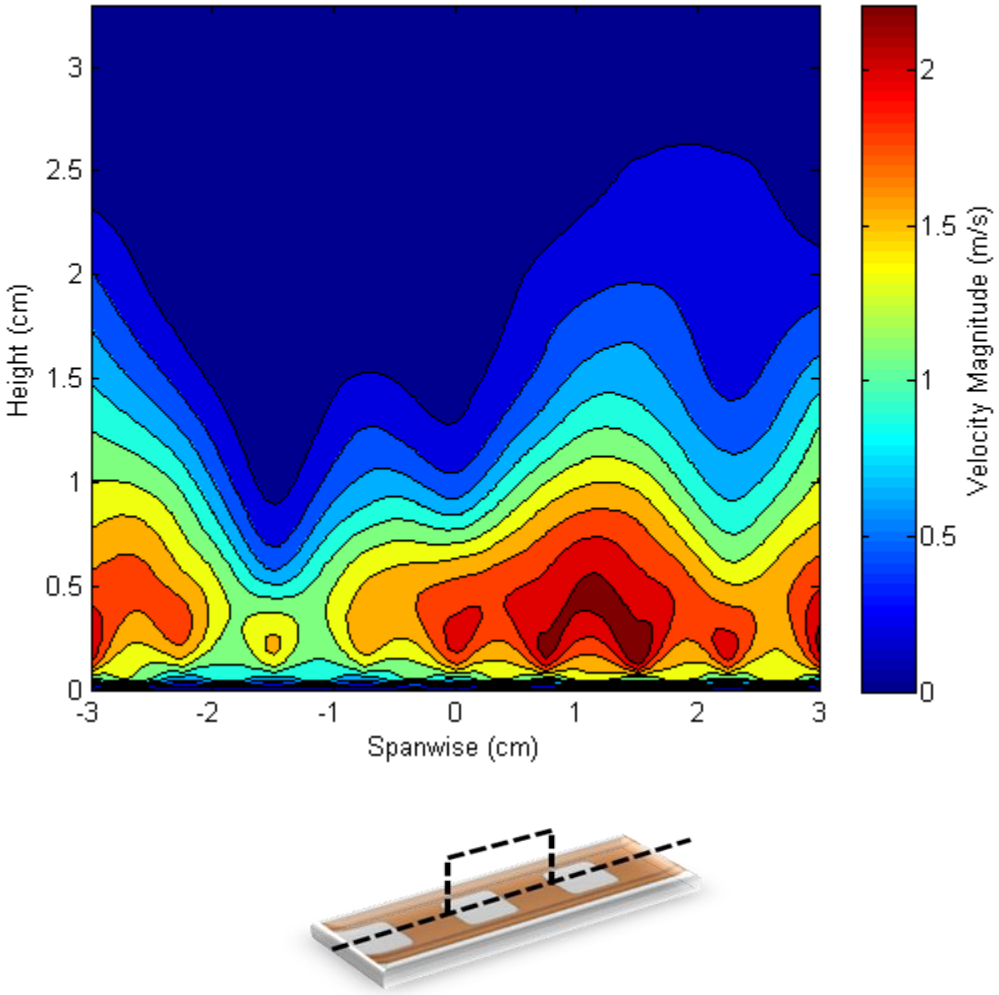

Figure 13: Experimental spanwise velocity distribution for one geometric wavelength.

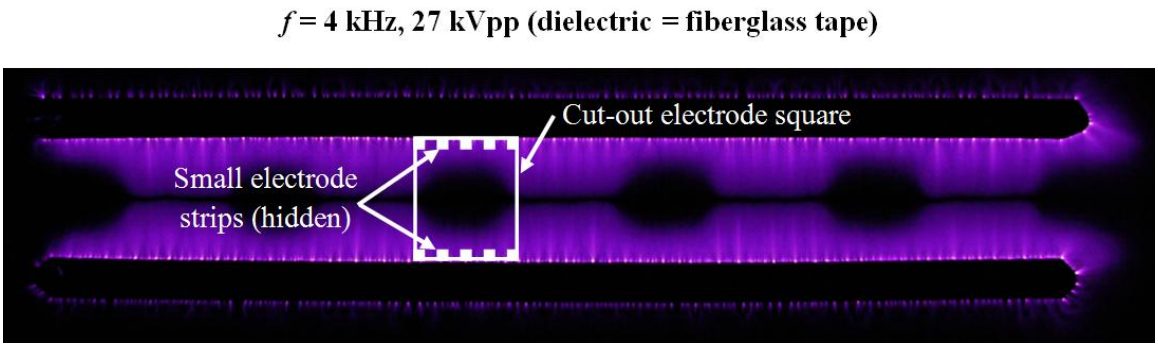

Figure 14: Image of binary actuator with regions of plasma formation shown in color.

If both effects are present, it is unclear which one is the greater driving factor for inducing velocity in that region. Images of the plasma actuator at various operating conditions (i.e., applied voltage and driving frequency) are included in Appendix B.

Virtual Electrode Correction

In order to compensate for the higher induced velocity in the cut-out electrode region than expected, the description of the buried electrode given by the Fourier series in Equation 6 must be modified. This is accomplished by introducing a "virtual electrode" in the regions where the physical electrode is cut out. In other words, the ambient fluid interacts with the adjacent plasma as if there was an electrode present in the cut-out region. The functional equivalent of the binary buried electrode originally given by (5) should instead be expressed as,

$$g(x) = \begin{cases} \beta & -\lambda_s/2 < x < 0 \\ w & 0 < x < \lambda_s/2 \end{cases} \tag{12}$$

where $0 < \beta < 1$. Recall that the Fourier series of $g(x)$ was normalized by the electrode width w, so that w may simply be replaced with a value of 1. Figure 16 illustrates the modified form of $g(x)$ with the virtual electrode correction factor.

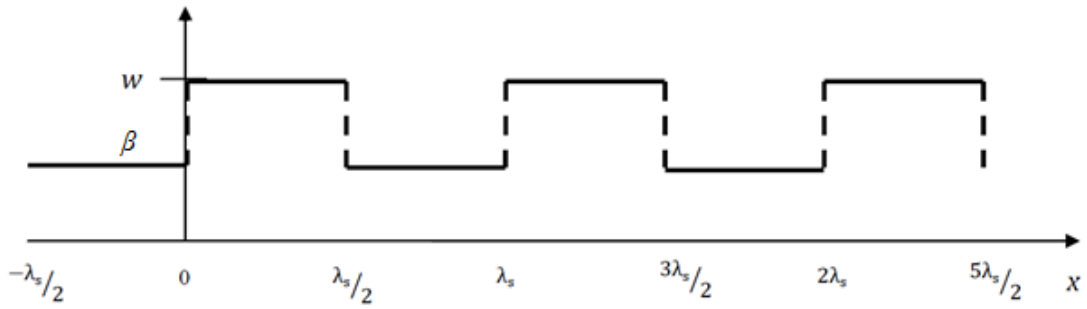

Figure 15: Shaping function with virtual electrode correction.

The value of β for the present case was chosen by trial-and error in order to closely approximate the maximum induced velocity distribution along the electrode span. Therefore, β was adjusted so that the "curve fit" to a single maximum induced velocity point (to be presented shortly) was within 95% confidence bounds; that is, the maximum induced velocity from the acquired cross-sectional velocity profile is used to adjust the value of β so that the maximum induced velocity described by the model closely matches the experimental data at that point to result in a best fit. A value of $\beta = 0.7$ was selected to achieve this in the present example. After recomputing the Fourier coefficients and applying the empirical coefficients for an applied voltage of 27 kVpp with $f = 4$ kHz, $d = 0.183$ cm, the resulting model given by Equation 2 yielded the induced velocity distribution in Figure 16.

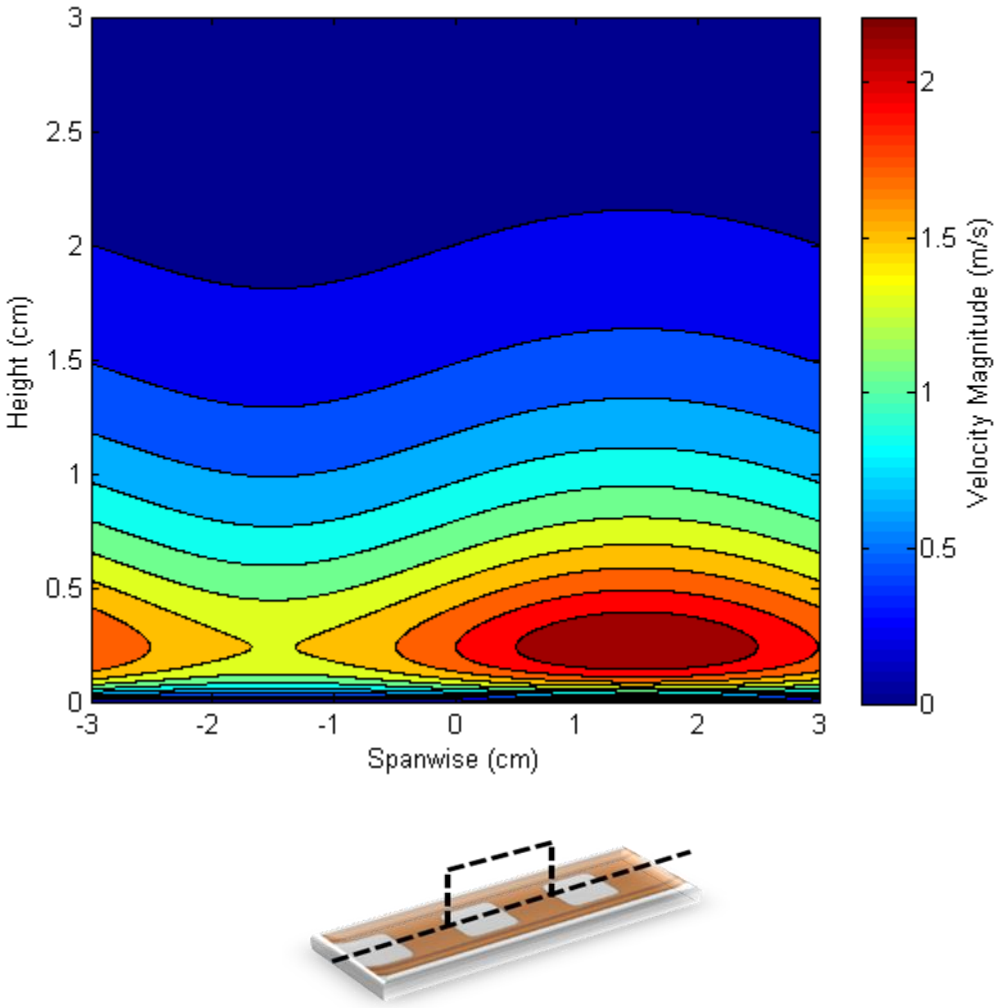

Figure 16: Virtual electrode model corresponding to experimental data.

A quantitative comparison between the empirical data, virtual electrode model, and original binary electrode model is cast in terms of the maximum induced velocity along the actuator span in Figure 17. Note that the Fourier series in each model consisted of a single term. The error bars for each data point are also shown, and illustrate the

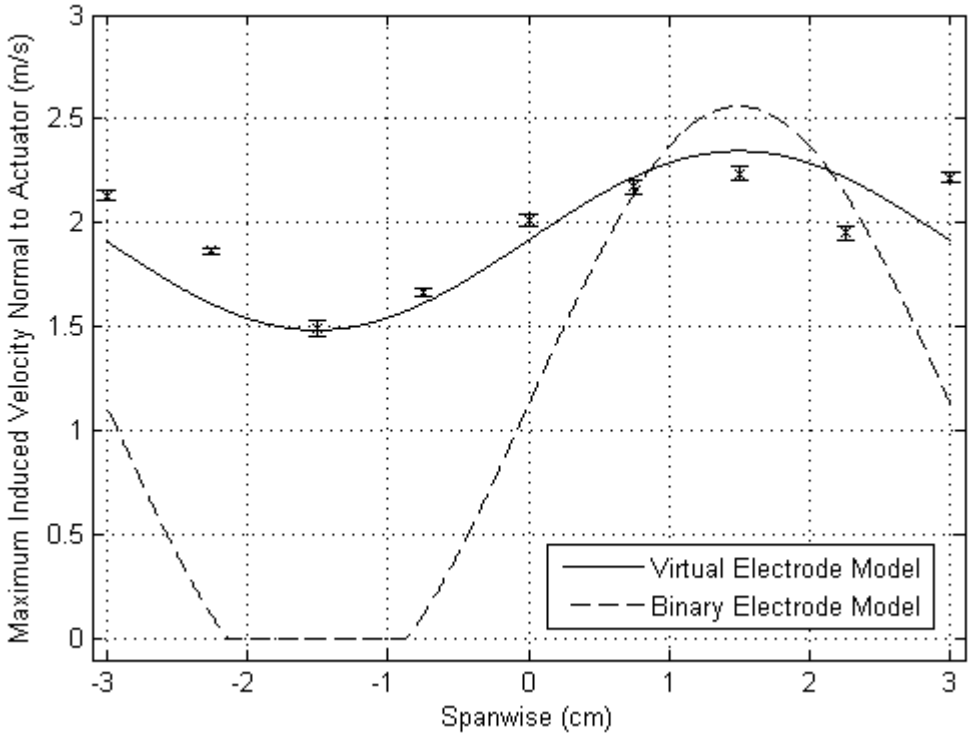

Figure 17: Comparison between the two considered models and experimental data.

small standard deviation of the pitot tube data under the block averaging scheme described in Chapter 3.

As Figure 17 powerfully illustrates, a viable flow-shaping plasma actuator model must account for the entrainment of fluid in regions where the electrode is cut out, since plasma formation does occur in the cut-out regions even if a small strip of electrode is present. The virtual electrode model is an attempt to compensate for this effect. From the proposed model given by Equation 2, the full description of the induced velocity magnitude normal to the centerline of the binary actuator with the virtual electrode

correction is given by,

$$V(x,y)=\left[\frac{1+\beta}{2}+\frac{2(1-\beta)}{\pi}\sin\left(2\pi\frac{x}{\lambda_s}\right)\right]\left\{\alpha_1\exp(\alpha_2 y)+\alpha_3\exp(\alpha_4 y)\right\} \qquad (13)$$

The first factor on the right-hand side of (13) represents the buried electrode description (shaping function) with the virtual electrode correction to account for fluid interaction above regions of cut-out electrode, and the second factor on the right-hand side of (13) is the curve fit to the cross-sectional velocity profile acquired normal to the wall at the location of maximum interacting plasma volume along the centerline of the buried electrode.

Chapter 5: Conclusions

In this work, the concept of a virtual electrode model was set forth to describe the distribution of velocity magnitude along the centerline of a binary flow-shaping plasma actuator in quiescent air. The effect of entrained fluid in cut-out regions of the buried electrode made it necessary to incorporate a correction in the modeling of the electrode geometry. This was addressed by imposing a "virtual electrode" in the cut-out regions, whereby the ambient fluid is accelerated as if there was a region of buried electrode present, since plasma does form there from the small strips of electrode required to preserve electrical continuity. The model was semi-empirical in nature, owing to the fact that a cross-section of velocity data as a function of height normal to the centerline of the actuator is acquired and then spatially modulated by a Fourier series description of the buried electrode geometry. The premise that the Fourier series was an appropriate shaping function in the modeling equation was shown to be satisfactory for the binary actuator, but it was not demonstrated whether a higher-order series for more elaborate buried electrode geometries is also appropriate. Ongoing work is focused on applying the Fourier series description to a triangular-shaped buried electrode to determine the degree to which the proposed model is generalized. Another point of study concerns the number of terms in the series which are sufficient to describe an arbitrary geometry while reducing the impact on the "waviness" of the velocity distribution. If the Fourier series is indeed an appropriate shaping function for the diamond actuator, then the proposed

method may be generalized to any arbitrary shape of the buried electrode as long as the fundamental geometry is periodic, since any periodic function may be expressed in terms of a Fourier series. The maximum induced velocity along the span of the fundamental square-wave geometry was found to correlate well with that described by the virtual electrode model. This observation is somewhat surprising, considering that only one cross-section of data could sufficiently describe the velocity at other spanwise stations.

The need for the virtual electrode correction in this study lends insight into the design of flow-shaping plasma actuators. If a large velocity gradient is desired for the transition from a region of cut-out electrode (such as to induce vorticity downstream of the actuator when placed in flow, for example), then the strip of electrode in this cut-out portion should be minimized as much as possible while preserving electrical continuity in order to reduce the volume of plasma (hence, induced velocity) formed there.

For implementation in a computational study, it is not unreasonable to consider modifying the model given by Equation 10 to a form similar to the blowing profiles in Equation 1, using the maximum induced velocity at the station (X, Z) as the forcing amplitude. Indeed, the experimental data indicated that the maximum induced velocity was less than 5 mm above the wall, so that the effect of the actuator may be simulated as a blowing slot. That is, the normal component of spanwise velocity may be expressible as,

$$V(x) = \max\{v(X, y, Z)\}\left[\frac{1+\beta}{2} + \frac{2(1-\beta)}{\pi}\sin\left(2\pi\frac{x}{\lambda_s}\right)\right] \tag{14}$$

Further work must be done in order to investigate whether such a computational approach results in an accurate simulation of the actuator when engaged in external flow. Modeling of the effect of the external flow (including both streamwise flow and crossflow) on the induced jet should be undertaken to support such an endeavor.

The proposed semi-empirical model may not be needed at all if a closed-form solution for the electrical power dissipated by the actuator as a function of its primary electrical and geometrical properties is determined, in which case the maximum induced velocity has previously been found by Enloe *et al*.[5] to vary as the seven-halves power of the rate of dissipated electrical energy. Although such a closed-form solution has been eluded to date, an improved understanding of the detailed physics relevant to the operation of the plasma actuator would be beneficial to this end.

References

1. Ahmed, A., and Bays-Muchmore, B., "Transverse flow over a wavy cylinder," Physics of Fluids, Vol. 4, No. 9, 1992, pp. 1959-1967.
2. Fish, F.E., and Battle, J.M., "Hydrodynamic design of the humpback whale flipper," Journal of Morphology, Vol. 225, 1995, pp. 51-60.
3. Kim, J., and Choi, H., "Distributed forcing of flow over a circular cylinder," Physics of Fluids, Vol. 17, No. 3, 2005, pp. 033103-1– 033103-16.
4. Gregory, J.W., Porter, C.O., and McLaughlin, T.E., "Circular Cylinder Wake Control using Spatially Distributed Plasma Forcing," 4th AIAA Flow Control Conference, AIAA 2008-4198, 2008.
5. Enloe, C.L., McLaughlin, T.E., VanDyken, R.D., Kachner, K.D., Jumper, E.J., Corke, T.C., Post, M.L., and Haddad, O., "Mechanisms and Responses of a Single Dielectric Barrier Plasma Actuator: Geometric Effects," AIAA Journal, Vol. 42, No. 3, 2004, pp. 595-604.
6. Pons, J., Moreau, E., and Touchard, G., "Asymmetric surface dielectric barrier discharge in air at atmospheric pressure: electrical properties and induced airflow characteristics," J. Physics D: Appl. Phys., Vol. 38, 2005, pp. 3635-3642.
7. Hall, K.D., Jumper, E.J., Corke, T.C., McLaughlin, T.E., “Potential Flow Model of a Plasma Actuator as a Lift Enhancement Device,” 43rd AIAA Aerospace Sciences Meeting and Exhibit, AIAA 2005-783, 2005.

8. Chen, F.F. *Introduction to Plasma Physics and Controlled Fusion, Volume 1: Plasma Physics*. Plenum, New York, 1984.
9. D. M. Orlov, "Modelling and simulation of single dielectric barrier discharge plasma actuators," Ph.D. Dissertation, University of Notre Dame, 2006.
10. Orlov, D.M., and Corke, T.C., "Electric circuit model for aerodynamic plasma actuator," 44th AIAA Aerospace Sciences Meeting and Exhibit, AIAA 2006-1206, 2006.
11. Porter, C.O., Abbas, A., Cohen, K., McLaughlin, T.E., and Enloe, C.L., "Spatially Distributed Forcing and Jet Vectoring with a Plasma Actuator," AIAA Journal, Vol. 47, No. 6, 2009, pp. 1368-1378.
12. Enloe, C.L., McLaughlin, T.E., VanDyken, R.D., Kachner, K.D., Jumper, E.J., and Corke, T.C., "Mechanisms and Responses of a Single Dielectric Barrier Plasma Actuator: Plasma Morphology," AIAA Journal, Vol. 42, No. 3, 2004, pp. 589-594.
13. Gregory, J.W., Enloe, C.L., Font, G.I., and McLaughlin, T.E., "Force Production Mechanisms of a Dielectric-Barrier Discharge Plasma Actuator," 45th AIAA Aerospace Sciences Meeting and Exhibit, AIAA 2007-185, 2007.
14. Tavoularis, S. *Measurement in Fluid Mechanics*. Cambridge University Press, 2005.

APPENDIX A: DATA REPEATABILITY AND UNCERTAINTY

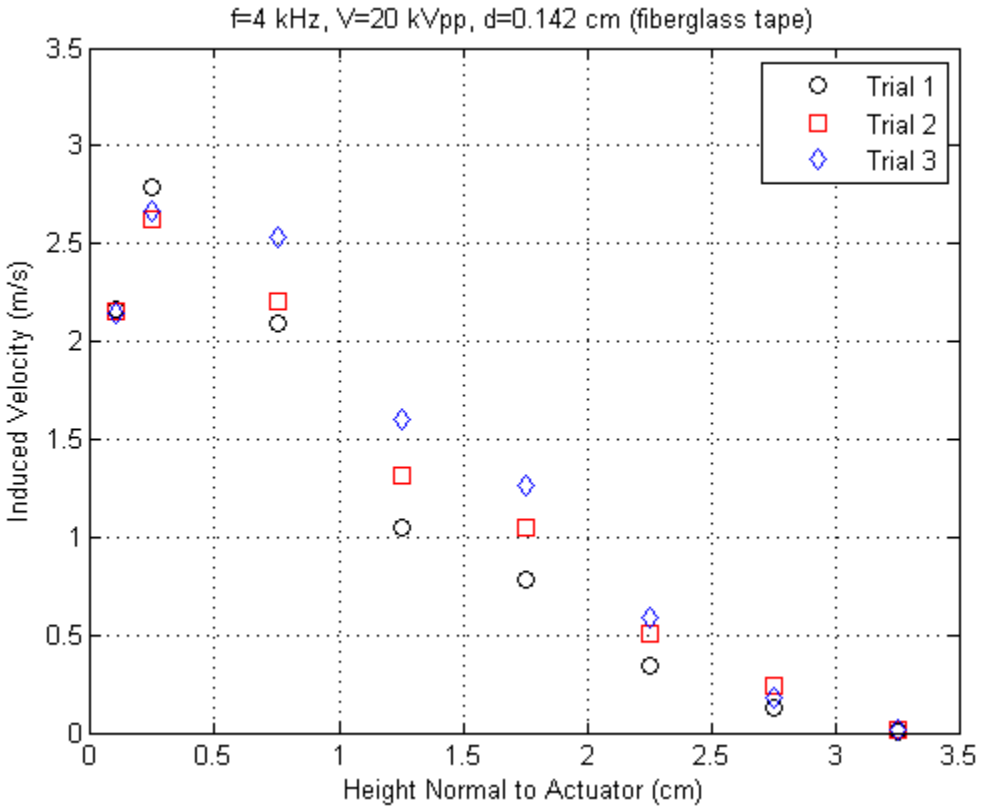

Figure 18: Repeatability for center electrode station, 15 sec time record (20 kVpp).

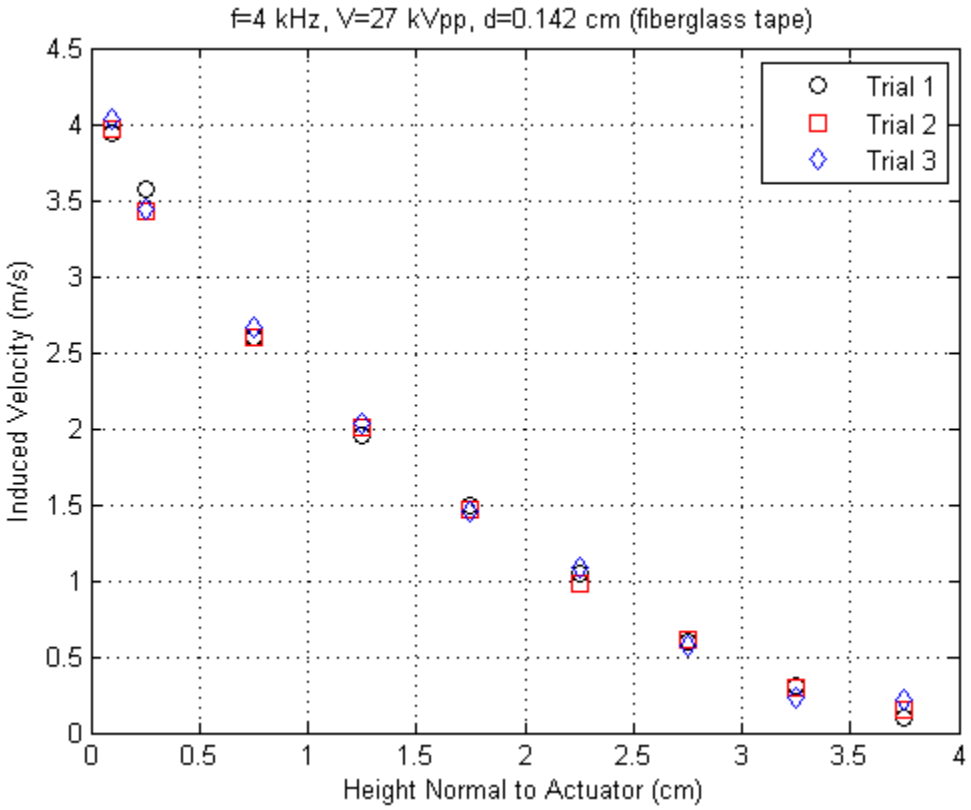

Figure 19: Repeatability for center electrode station, 15 sec time record (27 kVpp).

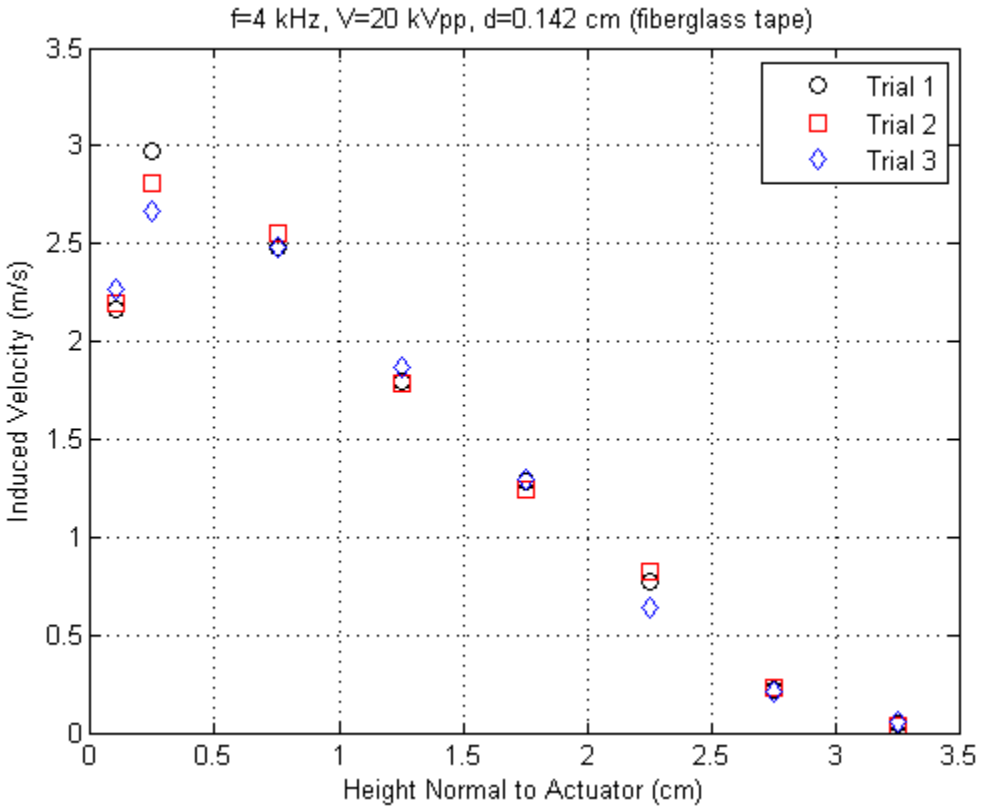

Figure 20: Repeatability for center electrode station, 30 sec time record (20 kVpp).

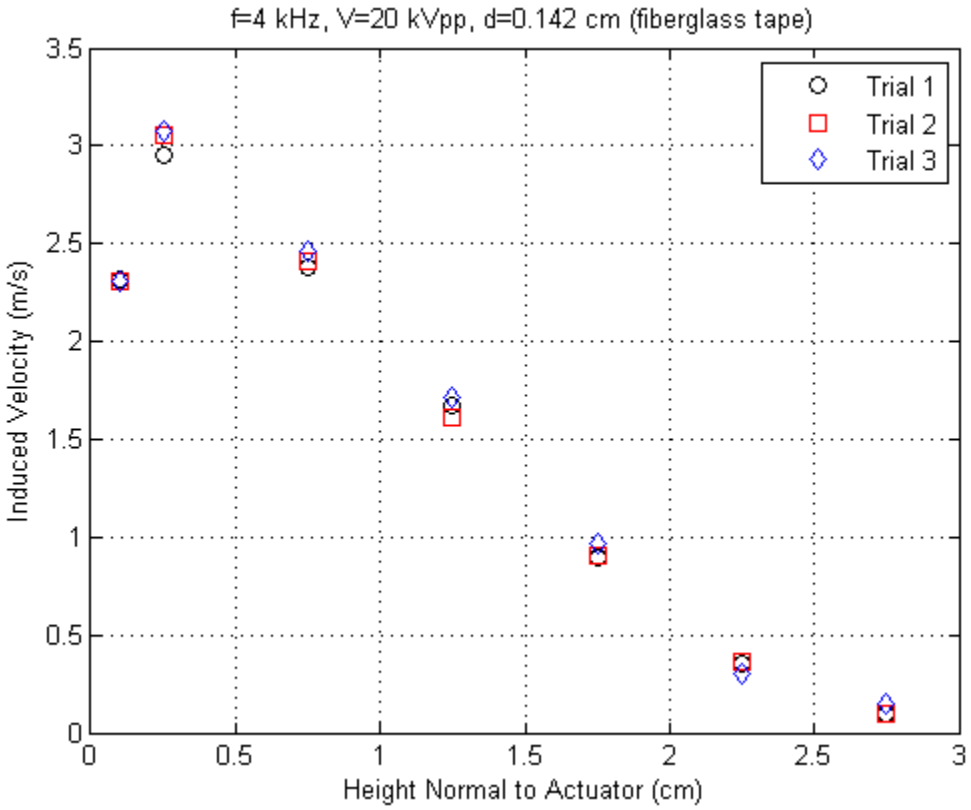

Figure 21: Repeatability for center electrode station, 45 sec time record (20 kVpp).

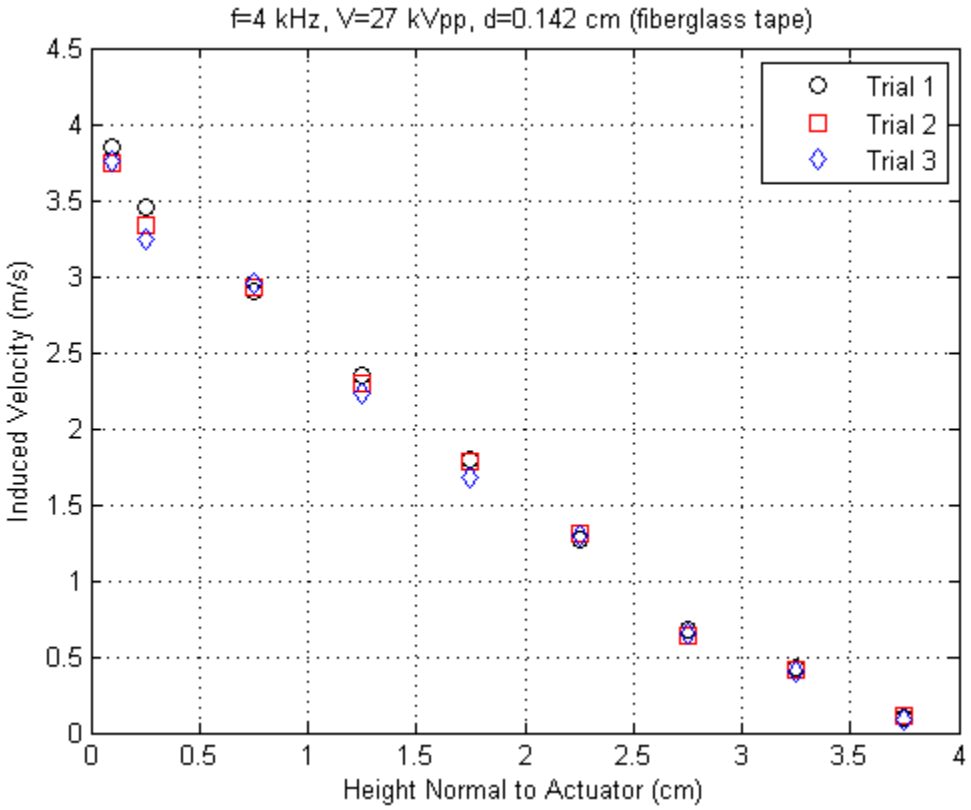

Figure 22: Repeatability for center electrode station, 45 sec time record (27 kVpp).

Table 3: Spanwise velocity data points and standard deviation.

***x* (cm)**	***y* (cm)**	**Induced velocity (m/s)**	**Standard deviation (m/s)**
-3	0	0	0
-3	0.1	1.76	0.02
-3	0.3	2.13	0.02
-3	0.6	1.73	0.02
-3	0.9	1.41	0.02
-3	1.2	1.14	0.02
-3	1.5	0.841	0.03
-3	1.8	0.601	0.05
-3	2.1	0.355	0.06
-3	2.4	0.156	0.05
-3	2.7	0.0445	0.02
-3	3	0	0
-3	3.3	0	0
-2.25	0	0	0
-2.25	0.1	1.25	0.01
-2.25	0.3	1.86	0.01
-2.25	0.6	1.50	0.02
-2.25	0.9	1.16	0.03
-2.25	1.2	0.713	0.05
-2.25	1.5	0.331	0.05
-2.25	1.8	0.135	0.03
-2.25	2.1	0.0254	0.02
-2.25	2.4	0.0807	0.03
-2.25	2.7	0.0412	0.03
-2.25	3	0	0
-2.25	3.3	0	0
-1.5	0	0	0
-1.5	0.1	1.28	0.01
-1.5	0.3	1.49	0.03
-1.5	0.6	0.575	0.05
-1.5	0.9	0.195	0.05
-1.5	1.2	0.0733	0.04
-1.5	1.5	0.0365	0.03
-1.5	1.8	0.0101	0.01
-1.5	2.1	0	0

x **(cm)**	***y*** **(cm)**	**Induced velocity (m/s)**	**Standard deviation (m/s)**
-1.5	2.4	0	0
-1.5	2.7	0	0
-1.5	3	0	0
-1.5	3.3	0	0
-0.75	0	0	0
-0.75	0.1	1.26	0.0
-0.75	0.3	1.66	0.01
-0.75	0.6	1.43	0.03
-0.75	0.9	0.833	0.04
-0.75	1.2	0.493	0.05
-0.75	1.5	0.218	0.03
-0.75	1.8	0.105	0.03
-0.75	2.1	0.041	0.02
-0.75	2.4	0.006	0.01
-0.75	2.7	0.005	0.01
-0.75	3	0	0
-0.75	3.3	0	0
0	0	0	0
0	0.1	1.635	0.01
0	0.3	2.01	0.02
0	0.6	1.63	0.04
0	0.9	0.689	0.07
0	1.2	0.250	0.05
0	1.5	0.151	0.04
0	1.8	0.097	0.03
0	2.1	0.047	0.03
0	2.4	0.016	0.01
0	2.7	0.007	0.01
0	3	0	0
0	3.3	0	0
0.75	0	0	0
0.75	0.1	1.92	0.01
0.75	0.3	2.17	0.03
0.75	0.6	1.96	0.04
0.75	0.9	1.51	0.04
0.75	1.2	0.908	0.04

x **(cm)**	***y*** **(cm)**	**Induced velocity (m/s)**	**Standard deviation (m/s)**
0.75	1.5	0.515	0.05
0.75	1.8	0.367	0.05
0.75	2.1	0.217	0.05
0.75	2.4	0.091	0.03
0.75	2.7	0.048	0.02
0.75	3	0	0
0.75	3.3	0	0
1.5	0	0	0
1.5	0.1	2.09	0.01
1.5	0.3	2.23	0.03
1.5	0.6	1.98	0.03
1.5	0.9	1.64	0.03
1.5	1.2	1.10	0.04
1.5	1.5	0.761	0.04
1.5	1.8	0.562	0.06
1.5	2.1	0.324	0.05
1.5	2.4	0.266	0.04
1.5	2.7	0.141	0.04
1.5	3	0.056	0.03
1.5	3.3	0	0
2.25	0	0	0
2.25	0.1	1.78	0.01
2.25	0.3	1.95	0.03
2.25	0.6	1.35	0.05
2.25	0.9	0.882	0.05
2.25	1.2	0.596	0.05
2.25	1.5	0.359	0.05
2.25	1.8	0.341	0.06
2.25	2.1	0.301	0.05
2.25	2.4	0.290	0.04
2.25	2.7	0.150	0.04
2.25	3	0.115	0.03
2.25	3.3	0.072	0.03
3	0	0	0
3	0.1	1.72	0.01
3	0.3	2.21	0.02

x **(cm)**	***y*** **(cm)**	**Induced velocity (m/s)**	**Standard deviation (m/s)**
3	0.6	1.83	0.02
3	0.9	1.43	0.03
3	1.2	1.18	0.03
3	1.5	0.780	0.04
3	1.8	0.472	0.05
3	2.1	0.223	0.04
3	2.4	0.104	0.04
3	2.7	0.071	0.03
3	3	0.024	0.02
3	3.3	0	0

APPENDIX B: IMAGES OF PLASMA FORMATION

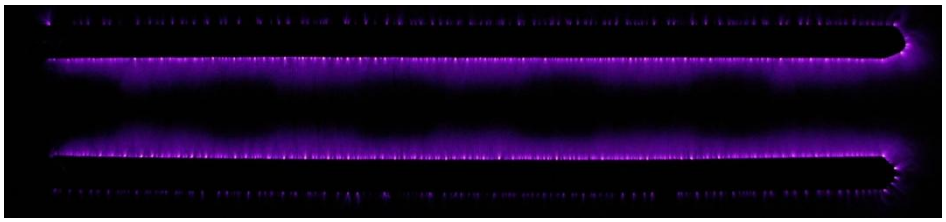

Figure 23: Plasma formation for binary actuator at 20.4 kVpp, 4 kHz.

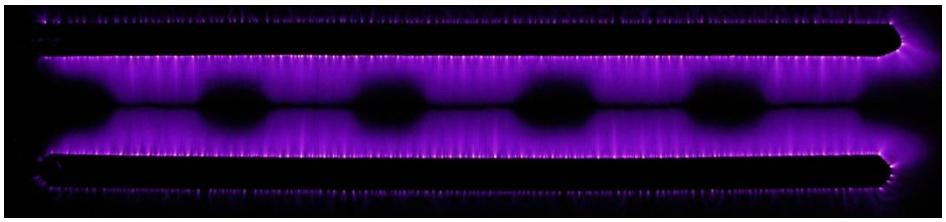

Figure 24: Plasma formation for binary actuator at 27 kVpp, 4 kHz.

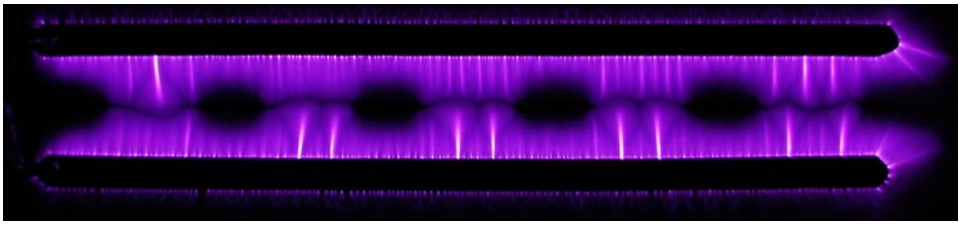

Figure 25: Plasma formation for binary actuator at 32.5 kVpp, 4 kHz.

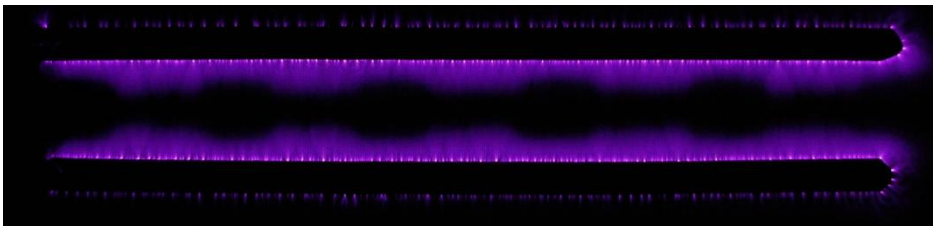

Figure 26: Plasma formation for binary actuator at 21.6 kVpp, 5 kHz.

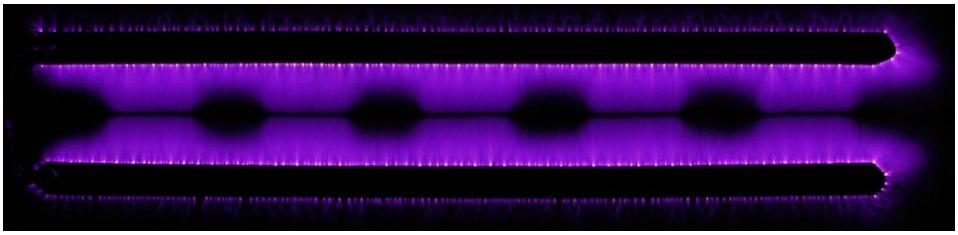

Figure 27: Plasma formation for binary actuator at 28.5 kVpp, 5 kHz.

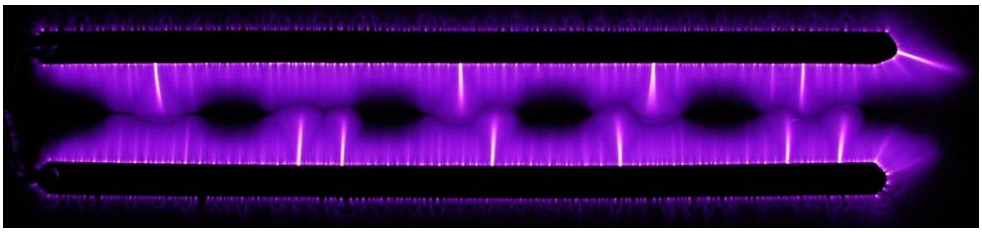

Figure 28: Plasma formation for binary actuator at 30.7 kVpp, 5 kHz.